Resistivity and full-decay IP inversion for imaging a coastal aquifer prone to saline intrusion: the Pontina Plain case study (Central Italy)

Running title: **ERT and full-decay IP for aquifer imaging**

Giorgio De Donno* and Michele Cercato

"Sapienza" University of Rome – DICEA Via Eudossiana 18, 00184 Rome, Italy

*Corresponding author: giorgio.dedonno@uniroma1.it

Publisher version: https://onlinelibrary.wiley.com/doi/full/10.1002/nsg.12259

Acknowledgments

This research is funded by 'Sapienza' University of Rome – Grant no. RM11916B7EE0A1A8/2019 (P.I. Giorgio De Donno). The authors wish to thank Francesco Pugliese ('Sapienza' University of Rome) and former M.Sc. students Michela di Rosa, Filomena Rondinelli and Alessandro Tomasella ('Sapienza' University of Rome) for their help during field acquisition. The Circeo National Park Authority and the Carabinieri Biodiversity Group (Reparto Carabinieri Biodiversità di Fogliano) are warmly thanked for permitting site access.

Conflict of interest

The authors declare that they have no conflicts of interest related to this work.

Abstract

Many coastal areas are affected by groundwater salinization due to the unsustainable use of groundwater resources. For a cost-effective quantitative assessment of groundwater resources, electrical resistivity tomography is often used as a standalone geophysical technique. In this paper, we present an application of the integration of direct-current electrical resistivity and full-decay induced polarization method at the Pontina Plain (Central Italy). The case study is a coastal area in Central Italy prone to salinization due to both geological and anthropogenic factors.

To achieve these goals, we inverted full-decay time-domain electrical data for Cole-Cole parameters. The resulting multi-parameter model provides a first approximation prediction of the permeability, employing well-established empirical relationships with the electrical parameters.

We demonstrated that our approach: i) can locate highly conductive zones directly related to saline intrusion inland using the resistivity as a fast proxy; ii) can remove the ambiguity in the detection of clay/silt layers in the near-surface and iii) permit a prediction of the permeability, employing full-decay inversion of time-domain electrical data. However, the extremely conductive environment prevents the use of induced polarization data for the reconstruction of deep layers or detection of the salt wedge front. Therefore, this approach can be used for hydro-geophysical screening and monitoring of salinization-prone sites, where strong limitations to direct inspection exist due to external constraints (e.g. protected lands).

Keywords: ERT; IP; hydrogeophysics; aquifer; permeability

Data availability statement

The data that support the findings of this study are available from the corresponding author upon reasonable request.

Introduction

The increasing global food production that occurred in the last decades has required an improvement in the diagnostic tools for monitoring agricultural and natural lands (FAO 2017). About 15% of the total land area has been affected by physical and chemical degradation, including soil and groundwater salinization (Wild 2003). However, only a limited number of maps are currently available in Europe and particularly in Italy, for areas subjected to salinization (Van Beek and Tóth 2012), even though it is well-known that large parts of the coastal territory have been damaged due to salinization.

Groundwater salinization is mostly due to pumping rates, which exceed the rate of natural recharge so that seawater is drawn into the aquifer to make up the deficit. In most cases, this is caused by the lack of planning and control of groundwater abstraction (Greene et al. 2016). Furthermore, climate change is expected to worsen and accelerate this phenomenon in Mediterranean regions, by reducing the total amount of rainfall, increasing extreme events, and causing sea level rise thus contributing to saline water intrusion inland (Cramer et al. 2020). The latest EU directives regarding water resources (EU Water Framework Directive 2000 and linked legislation) require good chemical and quantitative status of groundwater to be achieved by 2027 at the latest. To this aim, electrical conductivity (EC), as well as its inverse electrical resistivity (ER), is recognized as a straightforward indicator of salinization, as high EC (low ER) values observed for shallow groundwater are a proxy for irreversible contamination (Greene et al. 2016).

During the last decades, well monitoring has been the most used approach for mapping vulnerability in coastal aquifers (Melloul and Goldenberg 1997). However, this approach can lead to ambiguous results if the sample collection is too sparse when compared to the variability in the subsoil. This scenario is frequent in Italy where the subsoil is often extremely heterogeneous and information about the subsoil layering is often available only at scattered points. In this case, the correlation between borehole data and areal information given by non-invasive techniques can help to retrieve a high-resolution model of the coastal areas without any damage to the environment (Paillet 2003). Therefore, ER monitoring can potentially represent a powerful and robust tool to image and monitor salinization-prone zones.

Electrical resistivity mapping of coastal aquifers has often been accomplished during recent years employing airborne electromagnetic (EM) methods (e.g. Siemon et al. 2019) or, where increased resolution is needed, using the electrical resistivity tomography (ERT) on selected profiles (e.g. Costall et al. 2018). However, using ERT as a standalone may not be the best choice in complex scenarios where resistivity ranges related to different lithotypes may overlap, mainly due to variations in clay content, salinity and saturation levels (Samouëlian et al. 2005).

Nowadays, the additional contribution given by the induced polarization (IP) technique is recognized to be pivotal for aquifer characterization, given the high polarization of clay minerals (Slater and Lesmes 2002). Therefore, the tomographic inversion of time-domain IP (TDIP) data has been an emergent techniquein recent years for many environmental applications (see Binley and Slater 2020 for a review). However, it has still rarely been applied for mapping saline intrusion or in coastal areas (Kumar et al. 2022), due to the low signal-to-noise ratio in such conductive environments. The TDIP data processing is generally performed by a rapid inversion using an integral chargeability value (Oldendurg and Li 1994), discarding the whole information contained within the IP decay curves. Recently, a new technique to improve the interpretation of IP surveys has been developped by extracting the spectral information through a full-decay IP analysis (Fiandaca et al. 2012). The full-decay IP analysis can be used for predicting key parameters (i.e. porosity, permeability, etc.) for coastal aquifers, given the relationship between real and imaginary components of the complex conductivity and the permeability or the porosity of unconsolidated sediments established in the laboratory with IP measurements on small samples (Weller et al. 2015).

In this work, we present an application of full-decay TDIP inversion at the Pontina Plain site (Lake Fogliano), which is a coastal area in Central Italy prone to salinization due to both geological and anthropogenic factors. We use electrical resistivity for mapping the salinization of coastal areas and polarization properties for predicting the hydrogeological parameters (permeability) of the shallow groundwater aquifers and aquicludes. To achieve the proposed goals, a new inversion algorithm implemented in Matlab and based on inequality constraints and log-10 transformed parameters is used as a tool to gain information on the site under investigation.

Methods

We use a full-decay TDIP 2.5D forward mapping, achieved by a Fourier transformation of the frequency-domain solver in the algorithm proposed by De Donno (2013) to solve for the complex electric potential. The forward code permits the modelling of the full-wave form of the electric potential, also incorporating the 50% duty cycle and the filter effect for IRIS Syscal instruments (used in the case study). We carry out data inversion for Cole-Cole (CC) parameters with a two-step Gauss-Newton algorithm, employing log-10 transformed parameters and inequality constraints. Using log-transformation in the parameterization implies that relative changes (e.g. also at low magnitudes) in a parameter value are equally weighted in the inversion (Kemna 2000). We incorporate in the inversion process the a priori information available in the study area through inequality constraints, which help to improve the model reconstruction and facilitate the inversion procedure, if the bounds are not too restrictive (Kim and Kim 2011). In this study, we take advantage from the knowledge of expected lithotypes from previous geological campaigns and we set the ranges for resistivity, chargeability and relaxation time values accordingly, while the frequency exponent is limited to 0.6 because it is never much above 0.5 for sandy and clayey materials (Revil et al. 2014).

Frequency-domain 2.5-D forward modelling

The resistive and capacitive response of a medium to external current stimulation is defined by Ohm's law:

$$\mathbf{J} = \frac{\mathbf{E}}{\rho^*(\omega)} = \frac{\mathbf{E}}{\rho'(\omega)+i\rho''(\omega)}\,, \tag{1}$$

where $i = \sqrt{-1}$, **J** and **E** are current density and electric field vectors and ρ^* is the complex electrical resistivity ($\sigma^* = 1/\rho^*$ is the complex conductivity), which generally depends on the angular frequency $\omega = 2\pi f$, being f the frequency. The real part of complex conductivity (σ') is related to the electrolytic conduction in the bulk pore solution, while the imaginary part (σ'') to the polarization mechanisms. For environmental applications operating in the low-frequency range (< 10^3 Hz), the polarization dominant mechanism is the polarization of the ionic charge associated with the electrical double layer (EDL) that exists at the mineral-fluid interface (Binley et al. 2005). We discard the electrode polarization effect, observed in presence of electronic conductors and utilized as a tool for mining exploration (Binley and Slater 2020), since we do not expect to encounter metals, pipes or other utilities in the National Park.

The frequency dependence of the complex resistivity is generally described by phenomenological models (e.g. Cole and Cole 1941; Pelton et al. 1978). The complex resistivity for the Cole-Cole (CC) model, widely used for geophysical purposes, is given by:

$$\rho^*(\omega) = \rho_0\left[1 - m_0\left(1 - \frac{1}{1+(i\omega\tau)^c}\right)\right], \tag{2}$$

where ρ_0 is the direct-current (DC) resistivity [Ωm], m_0 is the intrinsic chargeability [dimensionless or mV/V], τ the relaxation time [s] and c the frequency exponent [dimensionless].

The resistive response of a 2.5-D subsoil (where conductivity varies only within the x-z plane, while the electric potential is three-dimensional distributed), is described within a domain *D* by the Fourier-transformed Poisson's complex equation under the hypothesis of an external point source located at (x_S, z_S):

$$-\nabla \cdot [\sigma^*(x,z,\omega)\nabla\phi^*(x,z,\lambda,\omega)] + \lambda^2\sigma^*(x,z,\omega)\phi^*(x,z,\lambda,\omega) = I^*\delta(x_S)\delta(z_S)\ \forall(x,z) \in D \qquad (3)$$

where, ϕ^* the electric transformed potential (complex-valued), λ the transformed variable, *I* the injected current and δ the Dirac's delta.

Eq. (3) is solved for each frequency in the range [10^{-4}, 10^{10}] using a logarithmic sampling with 5 points per decade and the finite-element method under Neumann- and Dirichlet-type boundary conditions given on surface, on lateral and bottom boundaries located "far enough" from the source, respectively (De Donno and Cardarelli 2017). The complex electrical impedance $Z_q{}^*(\omega_j)$ is then obtained by the superimposition of potential distribution pertained to a single quadrupole $q = 1, \dots, N_q$ and angular frequency ω_j ($j = 1, \dots, N_f$), being N_q the number of quadrupoles and N_f the number of frequencies. The DC response $Z_q(0)$ is computed using the same procedure for ω = 0.

Time-domain transform and waveform modeling

The TD step-off response $V^{S-OFF}(t)$ is derived at any time *t* > 0 after the current switch-off through an inverse Fourier sine transform of the frequency-domain response (Fiandaca et al. 2013):

$$V_q^{S-OFF}(t) = Z_q(0) - \frac{2}{\pi}\int_0^\infty \mathrm{Im}\left(-\frac{Z_q{}^*(\omega)}{i\omega}\right)\sin(\omega t)\,\mathrm{d}\omega\ , \qquad (4)$$

where the integral in (4) is evaluated in terms of a Fast Hankel transform, for 20 fixed log-spaced values of the variable *t* between 0.01 and 8 s, by developing and parallelizing the Matlab code after Ingeman-Nielsen and Baumgartner (2006), based on the filter values by Christensen (1990). The frequency-domain response is interpolated to 10 points per decade through cubic splines for ensuring the accuracy of the Hankel transform. Then we compute the real stacked potential by superimposing alternating pulse with proper signs, also modelling the 10 Hz analogue filter implemented to reduce noise on the IRIS Syscal Pro resistivity-meter (used in the field survey). In this work, the solution is given for 2 s of on-time and off-time periods and 2 stacks with opposite polarity (50% duty cycle), which is a common configuration for field surveys, also adopted in our field survey.

The numerical forward solution was compared with the analytical solution after Pelton et al. (1978) using a simple homogeneous model. The results (Fig. 1) show low errors ~0.01%, also for increasing decay times.

Inversion procedure

Our protocol encompasses a two-step procedure: firstly, we determine resistivity ρ and integral chargeability η models through a fast ERT/IP inversion using the linear approximation of Oldenburg and Li (1994), as implemented in the VEMI algorithm by De Donno and Cardarelli (2017). The obtained chargeability model is normalized by the resistivity (normalized chargeability - MN) to separate the surface polarization contribution from the bulk conduction (Slater and Lesmes 2002).Then, the spectral inversion is performed using the CC model ($m_k = [\rho_{0k}; m_{0_k}; \tau_k; c_k]$, $k = 1, 2, \ldots, M$ with M the number of elements). Starting ρ_0 and m_0 models are chosen to be the ρ and η models achieved at the last iteration using the fast ERT/IP inversion, while initial constant values for τ and c are set to 1 s and 0.3, respectively. Inequality constraints are set on model parameters such that: $\mathbf{a}_k < \mathbf{m}_k < \mathbf{b}_k$, with $\boldsymbol{a}_k = (0.1\ \Omega\text{m}, 0.1\ \text{mV/V}, 0.001\ \text{s}, 0.1)$ and $\mathbf{b}_k = (10^4\ \Omega\text{m}, 500\ \text{mV/V}, 5\ \text{s}, 0.6)$. We discard unrealistic values or values inconsistent with the near-surface geological scenario encountered for coastal areas. The log-transformed model vector is $\mathbf{x}_k = \log_{10}\left(\frac{\mathbf{m}_k - \mathbf{a}_k}{\mathbf{b}_k - \mathbf{m}_k}\right)$, with k=1,2, …, M.

The dataset is expressed for each quadrupole in terms of stacked electric potential (Fiandaca et al. 2012), measured before (referred to as DC voltage) and after (IP voltage) the current switch-off at the different time gates $i = 1, 2, \ldots, N_g$ ($\mathbf{d} = [V_q^{DC}, V_{q,i}^{IP}]$).

We employed a Gauss-Newton iterative formulation for inverting TDIP data for CC parameters, where the modified model update vector $\delta\mathbf{x}$ is calculated by:

$$\delta\mathbf{x}^{(n)} = [(\mathbf{P}^{\mathrm{T}}\mathbf{J})^{\mathrm{T}}\,\mathbf{W}^{\mathrm{T}}\mathbf{W}(\mathbf{P}^{\mathrm{T}}\mathbf{J}) + \beta^{(n)}\mathbf{R}^{\mathrm{T}}\mathbf{R} + \lambda^{(n)}\mathbf{I}]^{-1}\{(\mathbf{P}^{\mathrm{T}}\mathbf{J})^{\mathrm{T}}\mathbf{W}^{\mathrm{T}}\mathbf{W}\big[\,\mathbf{d} - g\big(\mathbf{m}^{(n)}\big)\big] - \beta^{(n)}\mathbf{R}^{\mathrm{T}}\mathbf{R}(\mathbf{m}^{(n)} - \mathbf{m}^{0})\}\,, \tag{5}$$

being $\mathbf{J}$ the Jacobian matrix, $\mathbf{P}^{\mathrm{T}} = \frac{\partial\mathbf{m}}{\partial\mathbf{x}} = \frac{\ln 10(\mathbf{b}-\mathbf{m})(\mathbf{m}-\mathbf{a})}{(\mathbf{b}-\mathbf{a})}$, $\mathbf{W} = \mathrm{diag}(\frac{1}{\mathbf{s}^2})$ the data weight matrix ($\mathbf{s}$ are the observed standard deviations), $\mathbf{R}$ the smoothness matrix (second-difference operator using the four neighbors of the k^{th} block), $\mathbf{I}$ the identity matrix, $g\big(\mathbf{m}^{(n)}\big)$ the predicted data vector and β and λ regularization parameters at the *n*-iteration.

Once the model update vector the new model $\mathbf{m}^{(n+1)}$is:

$$\mathbf{m}^{(n+1)} = \frac{\mathbf{a}\big(\mathbf{b}-\mathbf{m}^{(n)}\big)+\mathbf{b}\big(\mathbf{m}^{(n)}-\mathbf{a}\big)e^{\ln 10\delta\mathbf{x}^{(n)}}}{\big(\mathbf{b}-\mathbf{m}^{(n)}\big)+\big(\mathbf{m}^{(n)}-\mathbf{a}\big)e^{\ln 10\delta\mathbf{x}^{(n)}}}\,. \tag{6}$$

The parameters β^{0} and λ^{0} are set to be equal to the initial misfit level and to $\max(\mathrm{diag}((\mathbf{P}^{\mathrm{T}}\mathbf{J})^{\mathrm{T}}\,\mathbf{W}^{\mathrm{T}}\mathbf{W}(\mathbf{P}^{\mathrm{T}}\mathbf{J}) + \beta^{0}\mathbf{R}^{\mathrm{T}}\mathbf{R}))$, respectively and then decreased at successive iterations by a cooling factor of 0.5, if the error decreases. Conversely, if error increases at the *n*-iteration, an inner loop starts with λ ranging from $\big[5\lambda^{(n-1)}, 0.1\lambda^{(n-1)}\big]$ and the optimal λ-value is chosen to be the highest value for which the error decreases. Usually from 5 to 15 iterations are required for achieving convergence of the process.

The Jacobian matrix $\mathbf{J}$ $[N_q \cdot \big(N_g + 1\big)\,x\,M]$ is calculated by using the same time-transform (eq. 4) used for the forward computation, where the FD Jacobian ($\mathbf{J}^{\mathrm{FD}}$) is derived by matrix multiplication of the FD sensitivity with the partial derivative of the complex resistivity with respect to the CC parameters using the chain-rule (see Kemna, 2000):

$$J_{q,k}{}^{FD} = \frac{\partial Z_q{}^{*}(\omega)}{\partial\rho_k{}^{*}(\omega)} \cdot \frac{\partial\rho_k{}^{*}(\omega)}{\partial m_k}. \tag{7}$$

We fully evaluate the complex-valued FD sensitivity for the first iteration using the procedure after De Donno (2013), then update sensitivity only for elements having cumulative sensitivity values higher than 10^{-5} (Nguyen et al. 2009), thus reducing the computational time by about 40%, without affecting significantly stability and convergence. We also apply parallel computation to speed up the computational time required by the TD transform of the Jacobian.

The comparison between numerical and analytical Jacobian is shown in Fig. 2 only for derivative with respect to m_0, τ e c (for DC resistivity Jacobian please refer to De Donno 2013). The comparison is made using the same homogeneous model as per the forward solution (Fig. 1). A maximum absolute error of 3.3% is obtained, which is enough to ensure convergence of the iterative process.

Permeability prediction

During recent years, empirical relationships between the hydraulic permeability k and induced polarization parameters have been derived in laboratory studies (e.g. Attwa and Gunther 2013) based on the strong connection between the imaginary component of the surface conductivity (σ''_{surf}) and the surface area normalized to the pore volume. Recently, Weller et al. (2015) directly correlated k and the electrical parameters investigating a large database of unconsolidated sediments:

$$k = 3.47 \cdot 10^{-16} \frac{\sigma_0(\sigma_f)^{1.11}}{\sigma''_{surf}(\sigma_f)^{2.41}}, \tag{8}$$

where $\sigma_0 = 1/\rho_0$ is the DC conductivity and σ_f the conductivity of a reference fluid equal to 100 mS/m.

Both σ_0 and σ''_{surf} should be corrected for the actual water conductivity and water chemistry (Weller et al. 2015). The value of σ''_{surf} should be calculated at 1 Hz. However, as shown by Fiandaca et al. (2018a), minor differences exist between $\sigma''_{surf}(f = 1\ Hz)$

and the maximum imaginary conductivity (σ''_{max}). Since σ''_{max} is directly linked to the CC parameters by (Fiandaca et al. 2018a):

$$\sigma''_{max} = \frac{-m_0 d}{\rho_0 (1-m_0)}, \quad (9)$$

with $d = \mathrm{Im}\left(\frac{1}{1+(1i)^c}\right)$, we derived it from inverted models, then using eq. (8) for predicting permeability.

Case study: the Pontina Plain (Central Italy)

Site description, data acquisition and processing

The study site is located near Lake Fogliano, the largest coastal lake of the Pontina Plain (Central Italy), included within the Circeo National Park with an area of about 5 km^2. This region presents a high variety of anthropogenic and natural factors whose combination has a great influence on the development and the extension of the salinization process, as stated in previous hydrogeological studies conducted close to the study area (e.g. Sappa and Coviello 2012). In addition to the climate changes and the rise in the mean sea level, reclamation activities of the last century led to the transformation of the wetlands into a plain (because of the limited elevations of the topography to the sea level) but also to a gradual settlement of population and economic activities in the coastal areas. These factors together with the lack of a sustainable management system of water resources cause groundwater qualitative and quantitative impoverishment, due to the loss of the dynamic interactions between fresh groundwater and seawater with high salt content. In recent years, rapid agricultural development and increased tourism activities have led to well-pumping rates not related to those of natural recharge and mapping aquifer vulnerability is now required.

The Pontina Plain is affected by a strong tectonic instability, which drove the deposition of Quaternary sediments (mainly sands but also clays, silts and gravels) in combination with the sea-level variations of the Quaternary glaciations. The study site hosts a multi-aquifer system: a near-surface unconfined aquifer, multiple confined deep aquifers and the basal aquifer in the calcareous bedrock (Manca 2014 and references therein).

Figure 3 shows the geological setting of the study area. The near-surface (0-60 m below the sea level) geology (Fig. 3a) is dominated by sandy deposits, which host different silt/clay content for thin layers at different depth and distance from the sea throughout the Plain (Fig. 3b). The transition between sands and marine clays is located at about 35-40 m b.s.l., but can be variable throughout the Plain. The lagoon silt (sandy silt) formation (depth: 0-10 m, with highly variable thickness in the site) is expected to amplify the IP response.

We found the water table in the well P (Fig. 3a) at shallow depths (~ 0 m b.s.l.), while the mean electrical conductivity of groundwater was between 0 and 5.5 m b.s.l. (maximum well depth) is around 130 mS/m (ρ_w ~ 7.5 Ωm), thus displaying a moderate salt content although being still labeled as freshwater. We assume that the materials below the maximum well depth are fully saturated by the same (salt-rich) freshwater and then by saltwater using hydrogeological information derived from neighboring deeper wells (Manca 2014). Surface waters located in the NW zone highlight higher salinization (between 1 and 30 g/l) compared to the SE area (< 1 g/l), according to electrical conductivity measurements performed within the Allacciante Canal (Manca 2014).

Five TD DC/IP lines were executed approximately normally to the seashore (Fig. 3), using the SyscalPro resistivity-meter, with 48 electrodes spaced 5 m apart and a multiple gradient array with a potential electrode separation a = [1,5] and a separation factor s = 9. The current electrode separation is $(s+2)\cdot a$ and therefore s represents the maximum number of potential readings for each current injection. The spatial distribution of the ERT lines was mainly constrained by the need to have proper coverage given the National Park's limitations to the geophysical survey. The multiple gradient array is chosen due to its efficiency in a multichannel acquisition system and because it minimizes the effect of electrode polarization (Dahlin and Zhou 2006).

Since the SyscalPro can collect only one standard deviation value in case of combined acquisition of DC and IP data (only related to the IP data) we performed an acquisition of a DC voltage dataset only and then a combined dataset with DC and IP decay voltages, to record a standard deviation value for both datasets. We set the amplitude of the input voltage to 400 V (for an example of voltage and current sections see supplementary material), with a current injection time of 2 s (2 stacks), a time delay of 20 ms and a logarithmic sampling of the IP decay curve using 20 gates (first gate centered at 30 ms, last gate at 1.75 s after current switch-off). We filtered raw data for outliers (clear isolated data points, data with a relative standard deviation from stacking measurements higher than 20%, where the latter threshold was set on the basis of empirical knowledge on high-conductivity environments), negative DC and/or IP voltage values or decay curves with increasing voltage. Only for full-decay inversion, unreliable IP decay curves were also canceled out, if large deviations between adjacent gates were displayed. At the end of inversion process, pixels having both low values (< 0.5%) of the model resolution matrix (MRM) and high values (> 0.1) of the depth of investigation (DOI) index at last iteration (see Caterina et al. 2013 for a review of the appraisal tools for electrical tomography) are discarded from the models.

For permeability prediction, we apply directly eq. (8) using σ''_{max} derived from the CC models instead of $\sigma''_{surf}(f = 1\,Hz)$ and without applying any corrections due to water conductivity and water chemistry. In fact, concerning the former effect, the conductivity logged in the P-well (average value of 130 mS/m) is close to that of the reference fluid and previous studies pointed out the minor effect of water conductivity changes on permeability estimation (Fiandaca et al. 2018b). The latter correction should take into account the effective mixture of cations and anions, even though the original suggestion is based on a sparse data set and numerous cations and anions are present in the field-collected water samples with varying molecular concentrations, so it is difficult to apply an appropriate correction.

Results

Preliminary results

The extremely high conductive environment in the NW zone (mean ρ~1.5 Ωm) leads to very low voltage signals recorded for the L1 and L2 lines, compared to the SW lines (mean ρ~15 Ωm), as shown in Fig. 4, where L2 dataset (Figs. 4a-d) is compared to L3 (Figs. 4e-h). Therefore, we restrict the DC/IP inversion only to L3, L4 and L5 datasets, while measurements acquired on L1 and L2 were inverted only for resistivity, discarding the IP datasets. For the L3 line, a strong 3D effect due to the bridge on the Allacciante Canal (x = 80-100 m) is also visible. Two electrodes were grounded directly on the bridge to cross the canal (approx. 8 m long), thus displaying an increased value of resistivity in the corresponding zone.

Since the maximum elevation observed is approximately 1 m a.s.l. for the L3, while L4 and L5 are located approximately at sea level, we can have a very thin unsaturated or partially saturated layer close to the surface having a maximum thickness of 1 m (the water table is located approximately at the sea level), where the results of the application of the permeability prediction can be biased.

Saline intrusion

The DC resistivity model for the L1 line (Fig. 5a) show approximately a four-layer model, where resistivity values vary in a high-conductive narrow range (0.5-2 Ωm), related to the presence of saltwater along the whole investigated line. The surface layer, which extends down to 3 m b.s.l., is extremely conductive (ρ < 0.5 Ωm), mainly due to fine-grained (clay and silt) marshy soil, peat with gravelly or pebbly fractions soaked in saltwater from the lake. Low resistivity values ($\rho < 1$ Ωm) were also found between 10 and 35 m b.s.l., due to saltwater-saturated sands. Conversely, a slight increase in resistivity is found between 3 and 10 m b.s.l. and from 35 m b.s.l. to the bottom of the model (ρ = 1-5 Ωm); this trend can be due to an increase in the fine fraction causing a variation of the electrical properties of these layers. The former layer can be associated with the lagoon silts, while the latter with the transition to the marine clays, both reported in the geological cross-section at comparable depths (Fig. 3). This layering is also confirmed on the L2 model (Fig. 5b), even though with some significant lateral variations. The most significant is the sharp increase of resistivity ($\rho > 5$ Ωm), highlighted from $x >$ 190 m (dashed white line in Fig. 5b), which is the transition surface between the salt wedge and the inland environment, where higher resistivity due to freshwater saturation is expected.

The L3 and L4 resistivity models (Figs. 6a and 6b) display a completely different electrical behavior (ρ = 5-100 Ωm), because of the absence of saltwater in these areas. Both lines can be interpreted as a four-layer model, where the resistive surface thin layer (0-2 m b.s.l.), is due to the vadose zone, as confirmed by the piezometric levels logged in the well P. Below, down to a depth of about 5-7 m b.s.l., the resistivity values vary between 5 and 15 Ωm, as of a water-saturated (with the above-mentioned conductive water) layer. Referring to the respective normalized chargeability models at the same depths (Figs. 7a and 7b), this layer can be the sandy silt layer (lagoon silt), as identified by the increase in normalized chargeability values (0.5-1 mS/m). Down to 35-40 m b.s.l., we found higher resistivity values (30-70 Ωm), without a significant IP effect, likely associated to the saturated sandy deposits, which overlie the marine clays in which a strong polarization is also visible. The effect of the canal on the L3 line is visible at x =80-

100 m, and it is also reflected in a higher RMS error (15%), due to an increased amount of noisy readings.

The surface layering of the L5 resistivity and normalized chargeability models (Figs. 6c and 7c) is comparable to the L3 and L4 ones, while a steep drop of resistivity (ρ < 5 Ωm) is seen below 12-15 m b.s.l. on the left part of the section (*x* < 120 m in Fig. 6c, dashed white line), due to the effect of the salt wedge intrusion inland. The right part of the L5 model, showing higher resistivity values (10-20 Ωm), can be related to brackish water (with a gradual reduction in saline content inland) or lithological changes, with an increase in the fine-grained fractions likely to be attributed to the marine clays, as previously shown on the L3 and L4 lines. The graphical reconstruction of the saline intrusion in the study area is depicted in Fig. 8, where the front of the salt wedge (ρ < 5 Ωm, white lines) is located approximately at a distance of 1.3-1.5 km from the seashore.

Near-surface aquifer characterization

Cole-Cole models are extended down to 35, 22 and 20 m for L3, L4 and L5 respectively, because of the above-mentioned further filtering procedure implemented for DC/IP voltage. Lower lateral resolution is also expected because the filtering procedure affects also the density of data points. Therefore, neither the high-conductive bottom left zone on the L5 line related to the saline intrusion nor the marine clays (L3-L4) were reached by these models.

The DC resistivity models (Figs. 9a, 10a and 11a) confirm the near-surface three-layer (resistive-conductive-resistive) geology at the site, except for the L3 line. In fact, in this model (Fig. 9a), the shallow layer shows high lateral variability, with transitions between the conductive to the resistive zone, already seen also in Fig. 6a.

The chargeability sections in Figs. 9b, 10b and 11b show low polarization for the bottom layer (as expected for clean sands), with a minor variability on L4 and L5 likely due to silt lenses within the sandy deposits. The thin shallow layer displays moderate (L5) to high (L3, L4) polarisation since it is expected to have a significant silt/clay fraction.

The τ sections (Figs. 9c, 10c and 11c) show a mean decay time around 0.9-1.1 s, slightly longer for L5 (1-1-1.3 s). Lower τ are reconstructed for the shallow (silty) layer on the L3 line ($\tau \sim 0.75$-1 s) and partially on the L4 (x = 120, 150 and 180 m), while this effect is not visible on L5. These differences are mainly related to the different grain sizes, since the relaxation time increases with grain size, even though the shorter decay times in the shallow soil could also be caused by the reduced water content (Binley et al. 2005).

The frequency exponent (Figs. 9d, 10d and 11d) is mostly in the range of 0.3-0.45, therefore showing low variability, with the highest c anomalies located in the shallow layer. Although these anomalies could correspond to a broader frequency spectrum, likely caused by different relaxation times due to clay/silt inclusions in a sandy background, this effect is likely due to the known correlation between c and m_0 (Madsen et al. 2017).

The resulting permeability cross-sections for the three lines, shown in Fig. 12, show low values (~10^{-12}-10^{-13} m^2 or less) for the sandy silt sediments, as expected, while higher values (10^{-10}-10^{-11} m^2) are found for beach and aeolian sands. The L5 line displays slightly lower k values, likely as an effect of low silty content within the sandy matrix.

Discussion

The investigation of saline intrusion in coastal aquifers is often conducted using electrical resistivity as the main proxy (e.g. Nguyen et al. 2009). As confirmed in this work, the DC resistivity is certainly a straightforward parameter to understand the physical processes undergo, since the highly conductive zones, where the resistivity is well below 5 Ωm, can be soundly attributed to saline intrusion. We chose a resistivity threshold of 5 Ωm for locating the saltwater-saturated sediments, which was previously used in similar coastal scenarios (e.g. Goebel et al., 2017). Nevertheless, ambiguity could arise in salt wedge detection since brackish water has similar resistivities of low permeable formations such as clay or silt (Choudhury and Saha 2004), as seen, for instance, in the L5 line (Fig. 6b) where we have a transition between salt wedge and clayey lithotype. Furthermore, the interpretation of the groundwater system as a whole should encompass also the reconstruction of the near-surface region including geological layering, detection of water table level and prediction of key hydraulic parameters such as permeability. In fact, in the Lake Folgiano area, the interpretation of the resistivity dataset alone may be unsatisfactory, mainly due to the high variability of the electrical response in the near surface due to different grain size distributions, porosity and saturation (Lesmes and Friedman 2005) related to changes in the fine-grained fraction of the shallow sediments of the Plain.

To these aims, IP methods have tremendous potential, as demonstrated particurarly by the L3 line (Fig. 9), since: i) normalized chargeability can be directly correlated to the magnitude of polarization phenomena, mainly driven by an increasing clay/silt content near surface, as for the sandy silt unit at a depth between 2 and 10 m or for the deep marine clays (depth > 30 m); ii) if the full voltage decay curves are properly modelled (e.g. with a CC model o better a CC re-parametrization) also petrophysical parameters can be inferred, but limited to the shallow layers (maximum DOI ~ 30 m) and only if the mean resistivity is much higher than 1 Ωm (only for lines L3, L4 and L5). In fact, where data are acquired in a highly conductive environment (i.e. L1 and L2 with mean resistivity ≈ 1-2 Ωm), such as close to the sea, the signal-to-noise ratio could be very low, thus preventing the acquisition of reliable decay curves at noteworthy depths, as demonstrated on the L2 line in this case and previously by other works (e.g. Bording et al. 2019). In such case, the effect of the decrease of ionic mobility becomes dominant with respect to the increase of charge density which prevails at lower salinity (see Binley and Slater 2020 for a review of the salinity dependence of IP measurements). This phenomenon is reflected in a slight reduction of the imaginary conductivity as a function of the salinity as previously observed for laboratory samples, in contrast with the increase observed for low-salinity values. Therefore, for a proper estimation of the formation factor or the surface conducitivity , multisalinity IP measurements should be collected, though which are unfeasible for surface-based applications of geophysical techniques (Weller et al. 2015). This is the main reason IP has rarely been applied in such geological scenarios. Conversely, where resistivity increases up to one order of magnitude, that is where TDIP lines are acquired inland or because the salt wedge is deeper (the case of L3-L4 and partly L5 lines with mean resistivity ≈ 15-35 Ωm), good quality TDIP data can be collected and a CC inversion can be feasible down to satisfactory depths (maximum DOI ~ 30 m).

We chose to invert TDIP data for CC parameters because the CC model is easy to implement and largely used in many geophysical applications. Since we invert TDIP data acquired in a narrow frequency range (time window = 20-2000 ms), we do not expect significant differences from inverting only for a constant phase value as per e.g. Flores-Orozco et al. (2022) or using the integral chargeability models of Fig. 6. Nevertheless, since the code is potentially valid also for other instruments and to deal with a wider frequency range, we present in this paper the full decay inversion for CC parameters. Where the classical CC model is chosen, m_0 and c are likely to be correlated (Madsen et al. 2017) and this can be reflected in a lower accuracy in the permeability estimation, mainly for areas where low c-values are observed (Maurya et al. 2018). Additionally, since the sensitivity of τ is lower compared to the other parameters (Fig. 2), also the expected DOI will be lower and interpretation is feasible only for the shallow layers. Moreover, since distinct fractions (sand, clay, silt) are likely to produce distinct relaxation times (Revil and Florsch 2010), that can be seen as multi-peaks on the SIP spectra and the CC model could not be able to fit well data in regions with strong grain size heterogeneity, as the shallowest layer in this case study. These disadvantages could be overcome in a future release of the code by replacing m_0 with i.e. σ''_{max} or ρ''_{min}, as proposed by Fiandaca et al. (2018a) and by implementing different models.

Nonetheless, the approach proposed in this paper still allows a reliable prediction of the permeability, since also eq. (8) is a semi-empirical model well calibrated and validated through measurements in controlled conditions spanning a wide range of unconsolidated sediments and therefore can be potentially applied to many geological scenarios with an approximate order of magnitude effectiveness. Other attempts to predict permeability through TDIP data with different approaches used in recent years (e.g. Revil et al. 2020), required the estimation of petrophysical parameters such as cementation exponent and grain density. Since these parameters are estimated through laboratory measurements on soil samples (Steiner et al. 2022), this method cannot be applied at the Circeo National Park, where drilling boreholes was unfeasible. Although the formation factor plays a critical role in the equations predicting hydraulic conductivity from induced polarization measurements (Flores-Orozco et al. 2022), it can be conveniently estimated in equation (8) by the low-frequency conductivity σ_0 (Weller et al. 2015). The advantage of the permeability prediction from TDIP data proposed in this paper is dual: i) lithology is better resolved in coastal areas since it is less sensitive to changes in fluid conductivity compared to imaginary conductivity or phase shift (Weller and Slater 2012) and ii) well-established permeability ranges are available in the literature for characterizing lithology, compared to the IP parameters (Maurya et al. 2018).

The achieved results for the case study presented in this paper are comparable to those reported by Weller et al. (2015): as an example, they reported values around 10^{-11} m^2 for sands, while permeability decreased to 10^{-13} m^2 for sand/clay mixtures and 10^{-14} m^2 for saprolites (50% sand, 30% silt and 20% clay). As a comparison, our formations show values of 10^{-10}-10^{-11} m^2 for the third layer (sand), while the permeability of the intermediate layer (sandy silt) is ~10^{-12}-10^{-13} m^2 or less, both consistent with previous results. On the other hand, the permeability of the shallow layer is extremely variable. As an example, for L3 very low permeability values (10^{-13} m^2 or less) are also extended to the shallow layer in the central area (x = 50-180 m) and also relaxation times are lower in these zones (< 1 s), likely because of the prevalence of the very fine fractions related to marshy clays and peats near surface instead of sandy sediments related to the beach sands. Moving towards the southeast direction (L4 and L5) there is a progressive increase of the coarse fraction as demonstrated by permeability increases to around 10^{-11} m^2.

A further improvement of these results, with much better areal coverage, can be achieved with a large-scale EM survey, even though the high variability of unconsolidated sediments in this geological scenario claims for high-resolution reconstruction of the near-surface layering, better achieved by ERT/IP methods.

Conclusions

We presented an integrated application of ERT and full-decay IP techniques for imaging saline intrusion and inferring petrophysical properties (permeability) on a coastal aquifer located in Central Italy. We demonstrated that the benefit of our approach is twofold: i) using the resistivity as a fast proxy can locate highly conductive zones directly related to saline intrusion inland; ii) integrating ERT models with IP data and spectral CC parameters can remove the ambiguity in the detection of clay/silt inclusions in the near-surface. Conversely, using IP for detecting salt wedges or reconstructing deep clay layers is not feasible due to the low signal-to-noise ratio observed in extremely conductive environments, such as those encountered in this geological scenario.

Although using CC parameters the chargeability models could be biased for low values of the frequency exponent, our results can be viewed as a first approximation reconstruction of the permeability, used for fast hydro-geophysical screening. These pieces of evidence should be validated by direct measurements even though at sites where drilling boreholes is strictly limited, as for protected lands like the Circeo National Park, the role of non-invasive methods is certainly predominant.

References

Attwa, M., Günther, T., (2013) Spectral induced polarization measurements for predicting the hydraulic conductivity in sandy aquifers. *Hydrol. Earth Syst. Sci.* 17(10), 4079-4094.

Binley, A., Slater, L.D., Fukes, M., Cassiani, G., (2005) Relationship between spectral induced polarization and hydraulic properties of saturated and unsaturated sandstone. *Water Resour. Res.* 41, W12417.

Binley, A., Slater, L.D., (2020) Resistivity and induced polarization: Theory and applications to the near-surface earth. Cambridge University Press.

Bording, T.S., Fiandaca, G., Maurya, P.K., Auken, E., Christiansen, A.V., Tuxen, N., Klint, K.E.S., Larsen, T.H., (2019) Cross-borehole tomography with full-decay spectral time-domain induced polarization for mapping of potential contaminant flow-paths. *J. Contam. Hydrol.* 226, 103523.

Caterina, D., Beaujean, J., Robert, T., Nguyen, F., (2013) A comparison study of different image appraisal tools for electrical resistivity tomography. *Near Surf. Geophys.* 11(6), 639-658.

Choudhury, K., Saha, D.K., (2004) Integrated geophysical and chemical study of saline water intrusion. *Groundwater* 42(5), 671-677.

Christensen, N.B., (1990) Optimized fast Hankel transform filters. *Geophys. Prospect.* 38(5), 545-568.

Cole, K.S., Cole, R.H., (1941) Dispersion and absorption in dielectrics I. Alternating current characteristics. *J. Chem. Phys.* 9(4), 341-351.

Costall, A., Harris, B., Pigois, J.P., (2018) Electrical resistivity imaging and the saline water interface in high-quality coastal aquifers. *Surv. Geophys.* 39(4), 753-816.

Cramer, W., Guiot, J., Marini, K., Secretariat, M., Bleu, P., (2020) Climate and environmental change in the Mediterranean Basin—current situation and risks for the future. First Mediterranean Assessment Report. Union for the Mediterranean, Plan Bleu, UNEP/MAP.

Dahlin, T., Zhou, B., (2006) Multiple-gradient array measurements for multichannel 2D resistivity imaging. *Near Surf. Geophys.* 4(2), 113-123.

De Donno, G., (2013) 2D tomographic inversion of complex resistivity data on cylindrical models. *Geophys. Prospect.* 61, 586-601.

De Donno, G., Cardarelli, E., (2017) VEMI: a flexible interface for 3D tomographic inversion of time- and frequency-domain electrical data in EIDORS. *Near Surf. Geophys.* 15, 43-58.

EU Water Framework Directive, (2000) Directive 2000/60/EC of the European Parliament and of the Council establishing a framework for the Community action in the field of water policy, 23 October 2000.

FAO, (2017) The future of food and agriculture–Trends and challenges. Annual Report 296, 1-180.

Fiandaca, G., Auken, E., Christiansen, A.V., Gazoty, A., (2012) Time-domain-induced polarization: Full-decay forward modeling and 1D laterally constrained inversion of Cole-Cole parameters. *Geophys.* 77(3), E213-E225.

Fiandaca, G., Ramm, J., Binley, A., Gazoty, A., Christiansen, A.V., Auken, E., (2013) Resolving spectral information from time domain induced polarization data through 2-D inversion. *Geophys. J. Int.*, 192(2), 631-646.

Fiandaca, G., Madsen, L.M., Maurya, P.K., (2018a) Re-parameterisations of the Cole–Cole model for improved spectral inversion of induced polarization data. *Near Surf. Geophys.* 16(4), 385-399.

Fiandaca, G., Maurya, P.K., Balbarini, N., Hördt, A., Christiansen, A.V., Foged, N., Bjerg, P.L., Auken, E., (2018b), Permeability estimation directly from logging-while-drilling induced polarization data. *Water Resour. Res.* 54(4), 2851-2870.

Flores-Orozco, A., Steiner, M., Katona, T., Roser, N., Moser, C., Stumvoll, M.J., Glade, T., (2022) Application of induced polarization imaging across different scales to understand surface and groundwater flow at the Hofermuehle landslide. *Catena* 219, 106612.

Goebel, M., Pidlisecky, A., & Knight, R. (2017). Resistivity imaging reveals complex pattern of saltwater intrusion along Monterey coast. Journal of Hydrology, 551, 746-755.

Greene, R., Timms, W., Rengasamy, P., Arshad, M., Cresswell, R., (2016) Soil and aquifer salinization: toward an integrated approach for salinity management of groundwater. In: *Integrated Groundwater Management* (pp. 377-412), Springer, Cham.

Ingeman-Nielsen, T., Baumgartner, F., (2006) CR1Dmod: A Matlab program to model 1D complex resistivity effects in electrical and electromagnetic surveys. *Comput. Geosci.* 32(9), 1411-1419.

Kemna, A., (2000) Tomographic inversion of complex resistivity: Theory and application. PhD thesis. Der Andere Verlag, Osnabrück.

Kim, H.J., Kim, Y., (2011) A unified transformation function for lower and upper bounding constraints on model parameters in electrical and electromagnetic inversion. *J. Geophys. Eng.* 8(1), 21-26.

Kumar, P., Tiwari, P., Biswas, A., Acharya, T. (2022) Geophysical investigation for seawater intrusion in the high-quality coastal aquifers of India: a review. *Environmental Science and Pollution Research* 30, 9127–9163.

Lesmes, D.P., Friedman, S.P., (2005) Relationships between the electrical and hydrogeological properties of rocks and soils. In: *Hydrogeophysics*, Springer, Dordrecht, pp. 87-128.

Madsen, L.M., Fiandaca, G., Auken, E., Christiansen, A.V., (2017) Time-domain induced polarization–an analysis of Cole–Cole parameter resolution and correlation using Markov Chain Monte Carlo inversion. *Geophys. J. Int.* 211(3), 1341-1353.

Manca, F., (2014) Study of seawater intrusion in the coastal areas of Circeo National Park and Litorale Romano Natural Reserve, for the implementation of numerical modeling methods. Ph.D. Thesis. Università Degli Studi Roma Tre. http://hdl.handle.net/2307/4368.

Maurya, P.K., Balbarini, N., Møller, I., Rønde, V., Christiansen, A.V., Bjerg, P.L., Auken, E., Fiandaca, G., (2018) Subsurface imaging of water electrical conductivity, hydraulic permeability and lithology at contaminated sites by induced polarization. *Geophys. J. Int.* 213(2), 770-785.

Melloul, A.J., Goldenberg, L.C., (1997) Monitoring of seawater intrusion in coastal aquifers: basics and local concerns. *J. Environ. Manage.* 51(1), 73-86.

Nguyen, F., Kemna, A., Antonsson, A., Engesgaard, P., Kuras, O., Ogilvy, R., Gisbert, J., Jorreto, S., Pulido-Bosch, A., (2009) Characterization of seawater intrusion using 2D electrical imaging. *Near Surf. Geophys.* 7(5-6), 377-390.

Oldenburg, D.W., Li, Y., (1994) Inversion of induced polarization data. *Geophys.* 59(9), 1327-1341.

Paillet, F., (2003) Spatial Scale Analysis in Geophysics — Integrating Surface and Borehole Geophysics in Groundwater Studies, In: *Spatial Methods for Solution of*

Environmental and Hydrologic Problems—Science, Policy, and Standardization, ed. V. Singhroy, R. Pierce, A. Johnson, and D. Hansen, West Conshohocken, PA: ASTM International, pp. 77-91.

Pelton, W.H., Ward, S.H., Hallof, P.G., Sill, W.R., Nelson, P.H., (1978) Mineral discrimination and removal of inductive coupling with multifrequency IP. *Geophys.* 43(3), 588-609.

Revil, A., Florsch, N., (2010) Determination of permeability from spectral induced polarization in granular media. *Geophys. J. Int.* 181, 1480–1498.

Revil, A., Florsch, N., Camerlynck, C., (2014) Spectral induced polarization porosimetry. *Geophys. J. Int.* 198, 1016–1033.

Revil, A., Ahmed, A.S., Coperey, A., Ravanel, L., Sharma, R., Panwar, N., (2020) Induced polarization as a tool to characterize shallow landslides. *J. Hydrol.* 589, 125369.

Samouëlian A., Cousin I., Tabbagh A., Bruand A., Richard G., (2005) Electrical resistivity survey in soil science: a review. *Soil Tillage Res.* 83(2), 173-193.

Sappa, G., Coviello, M.T., (2012) Seawater intrusion and salinization processes assessment in a multistrata coastal aquifer in Italy. *J. Water Resour. Prot.* 4(11), 954-967.

Siemon, B., van Baaren, E., Dabekaussen, W., Delsman, J., Dubelaar, W., Karaoulis, M., Steuer, A., (2019) Automatic identification of fresh–saline groundwater interfaces from airborne electromagnetic data in Zeeland, the Netherlands. *Near Surf. Geophys.* 17(1), 3-25.

Slater, L.D., Lesmes, D., (2002) IP interpretation in environmental investigations. *Geophys.* 67(1), 77-88.

Steiner, M., Katona, T., Fellner, J., Flores-Orozco, A., (2022) Quantitative water content estimation in landfills through joint inversion of seismic refraction and electrical resistivity data considering surface conduction. *Waste Manage.* 149, 21-32.

Van Beek, C.L., Tóth, G., (2012) Risk assessment methodologies of soil threats in Europe. JRC Scientific and Policy Reports EUR, 24097.

Weller, A., Slater, L., (2012) Salinity dependence of complex conductivity of unconsolidated and consolidated materials: Comparisons with electrical double layer models, *Geophys.* 77, D185–D198.

Weller, A., Slater, L., Binley, A., Nordsiek, S., Xu, S., (2015) Permeability prediction based on induced polarization: insights from measurements on sandstone and unconsolidated samples spanning a wide permeability range. *Geophys.* 80, D161–D173.

Wild. A., (2003) Soils, land and food: managing the land during the twenty-first century. Cambridge University Press, UK.

List of Figures

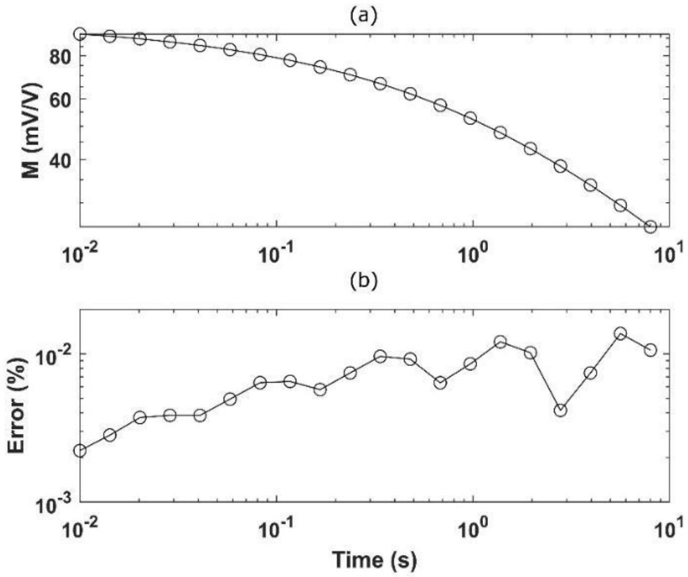

Figure 1. *Accuracy of the numerical solution tested for a model with* $\rho_0 = 1\ \Omega m$; $m_0 = 100\frac{mV}{V}$; $\tau = 2\ s$; $c = 0.5$. *(a) Comparison between numerical (solid line) and analytical (circle points) solution after Pelton et al. (1978), (b) Percentage absolute error.*

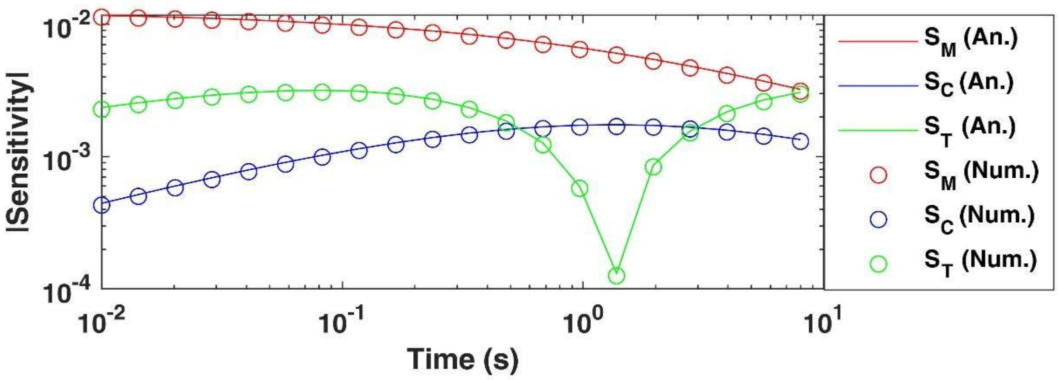

Figure 2. *Accuracy of the Jacobian calculation tested for a model with unitary DC resistivity and* $m_0 = 100\frac{mV}{V}$; $\tau = 2\ s$; $c = 0.5$. *Subscripts M, T and C indicate sensitivities calculated for* m_0, τ *and c respectively. (a) Comparison between numerical (solid line) and analytical (circle points) solutions after Pelton et al. (1978), for chargeability (red), relaxation time (blue) and frequency exponent (green).*

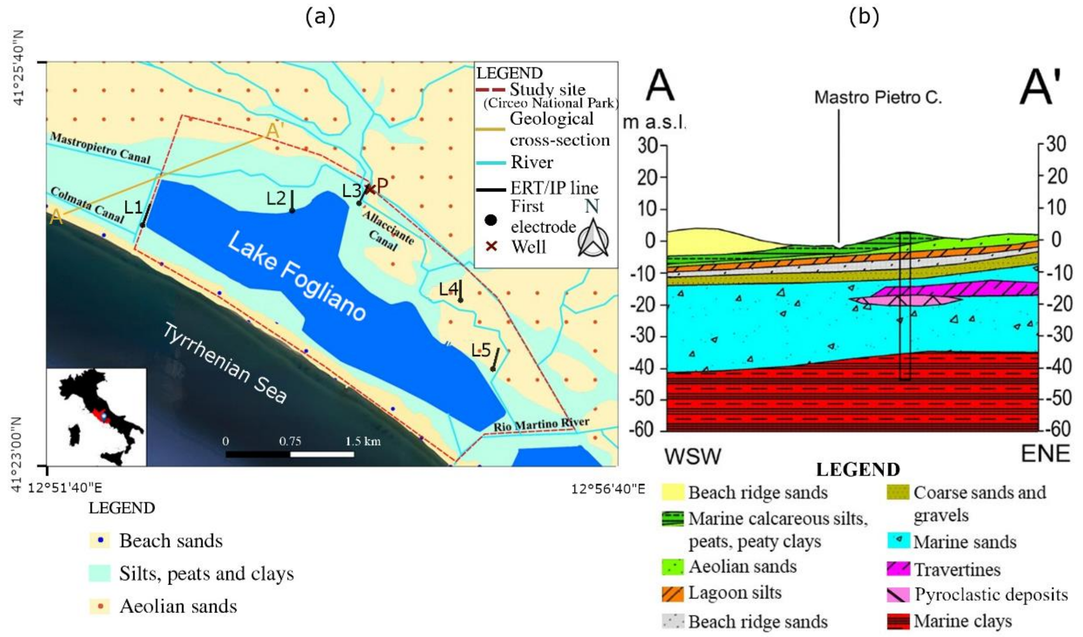

Figure 3. *Hydrogeological setting of the study area. (a) Geological map where TD ERT/IP lines are superposed (black solid lines). (b) A-A' geological cross*-section *(after Manca 2014, modified).*

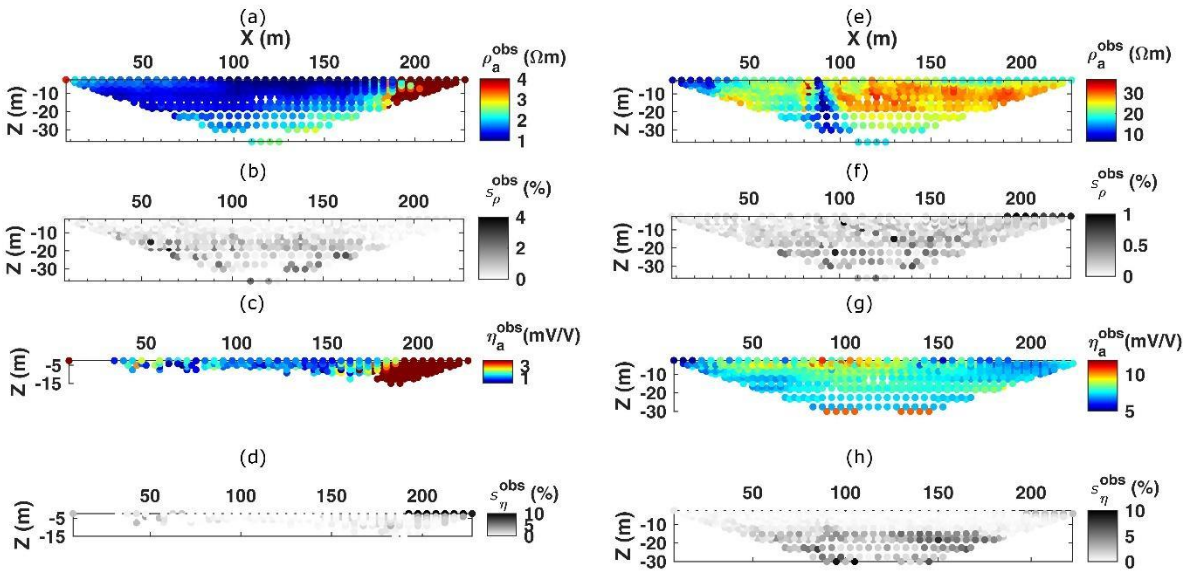

Figure 4. *Example datasets: L2 (a-d), L3 (e-h), plotted in terms of apparent resistivity and chargeability and related errors. Apparent resistivity values (a and e) and related standard deviations (b and f); apparent chargeability values (c and g) and related standard deviations (d andh).*

689

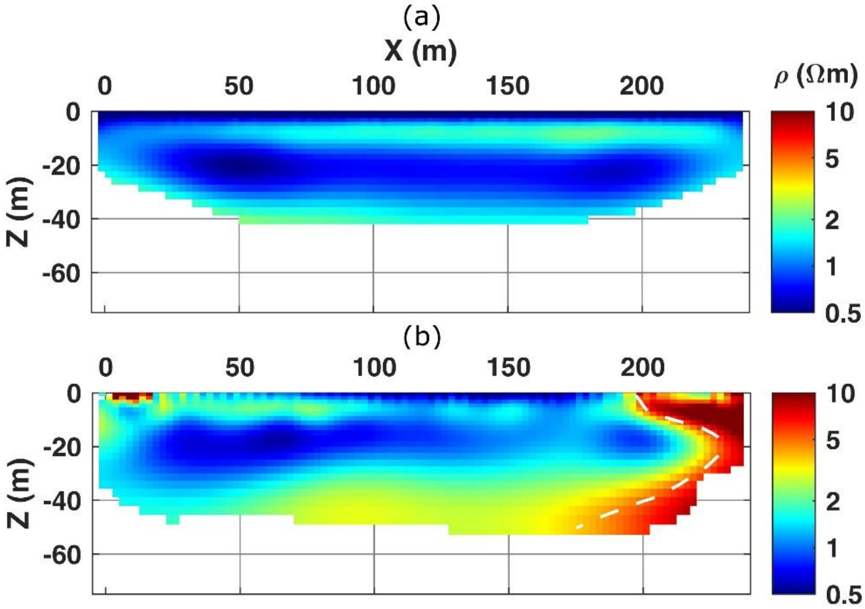

690 Figure 5. *Resistivity models for the L1 (a) and L2 (b) lines. RMS error is 1.78 and 2.28%*
691 *respectively. The limit of saline intrusion inland (ρ < 5 Ωm) is marked with the white*
692 *dashed line. White pixels are discarded due to low values of MRM and DOI.*

693

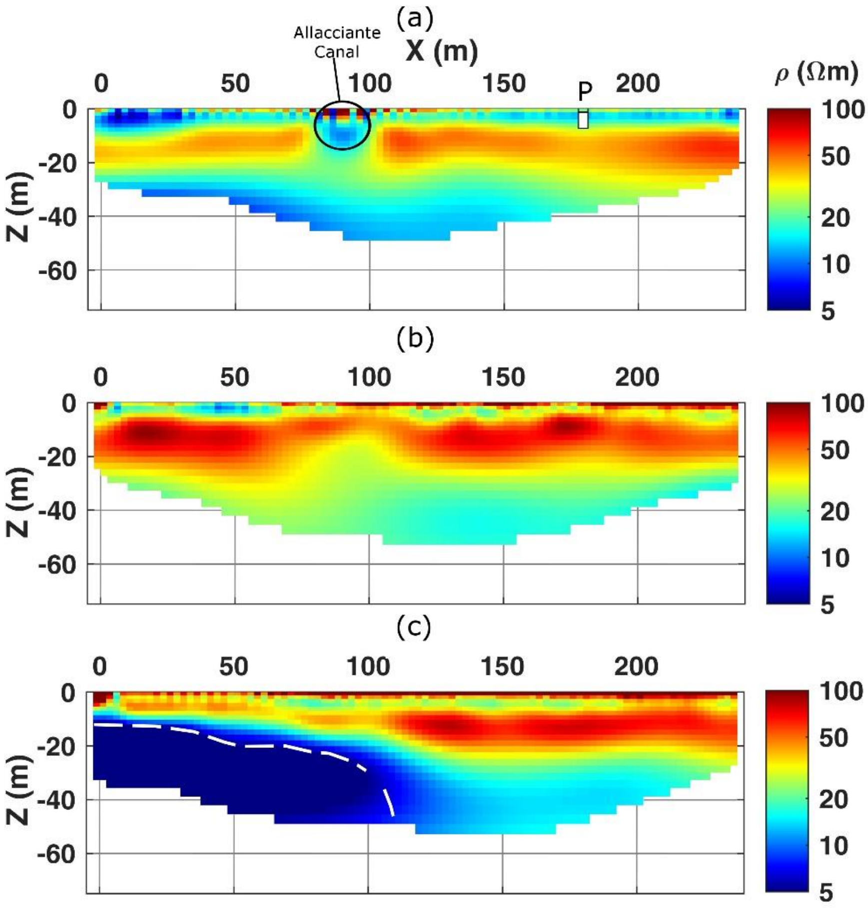

Figure 6. *Resistivity models for the L3 (a), L4 (b) and L5 (c) lines. RMS error is 15.14, 2.88 and 7.31%, respectively. The limit of saline intrusion inland (ρ < 5 Ωm) is marked with a white dashed line. White pixels are discarded due to low values of MRM and DOI.*

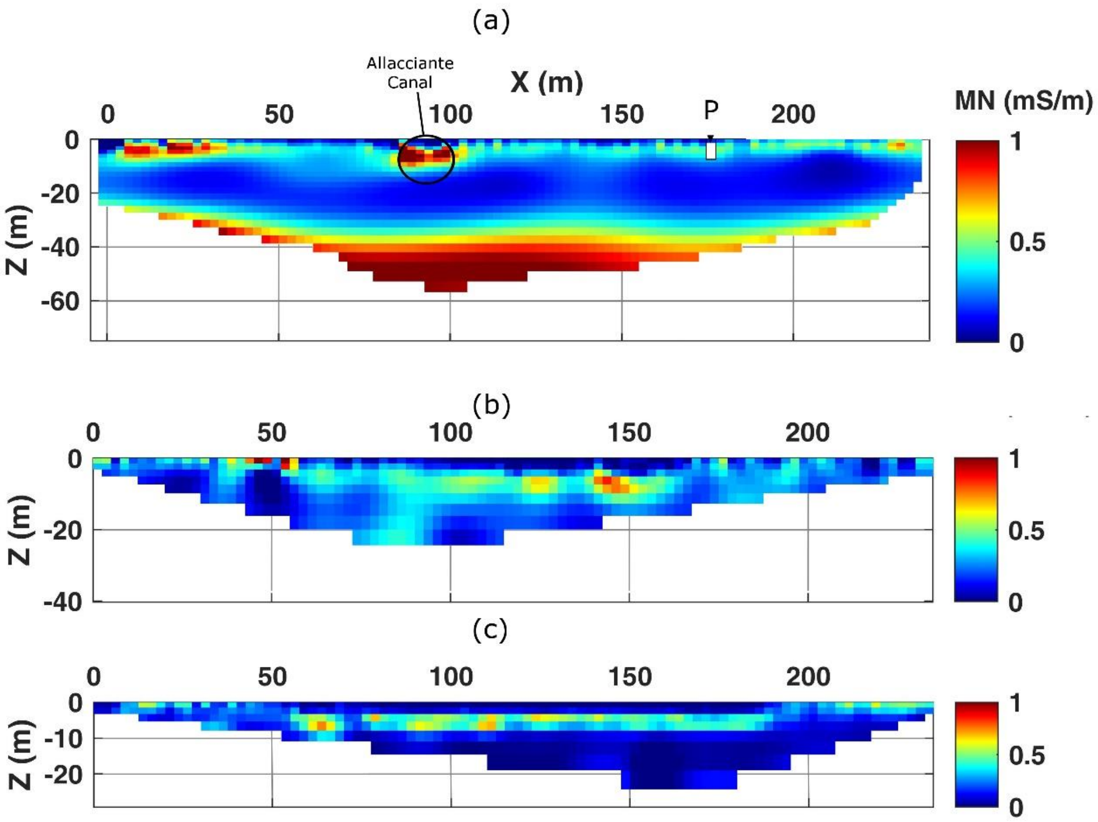

Figure 7. *Normalized chargeability models for the L3 (a), L4 (b) and L5 (c) lines. RMS error is 0.68, 1.78 and 0.84 mV/V, respectively. White pixels are discarded due to low values of MRM and DOI.*

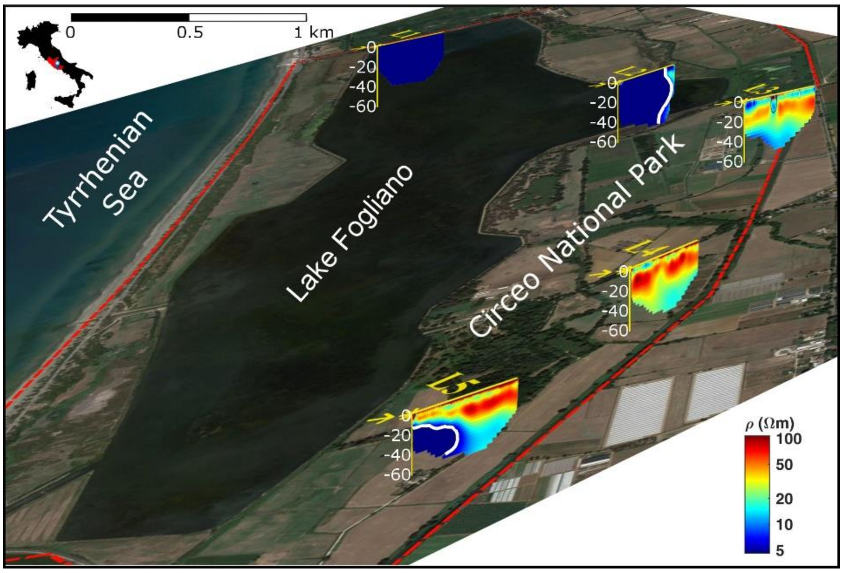

Figure 8. ERT lines at the Lake Fogliano. White lines indicate the limit of saline water intrusion inland (dark blue pixels). The depths are in meters.

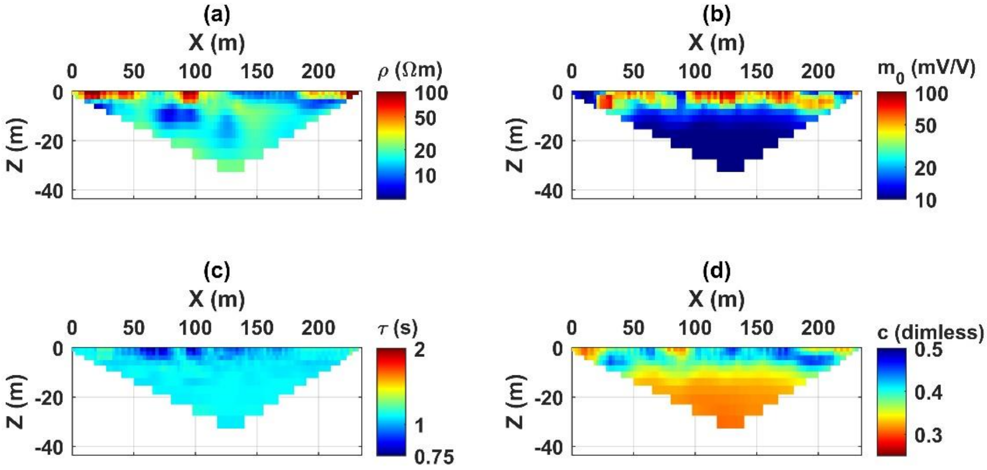

Figure 9. *Cole-Cole spectral inversion of the L3 line. (a) DC resistivity, (b) chargeability, (c) relaxation time, (d) frequency-exponent. RMS error is 10.26 mV for DC voltage and 0.37 mV for IP voltage. Vertical exaggeration is 2.*

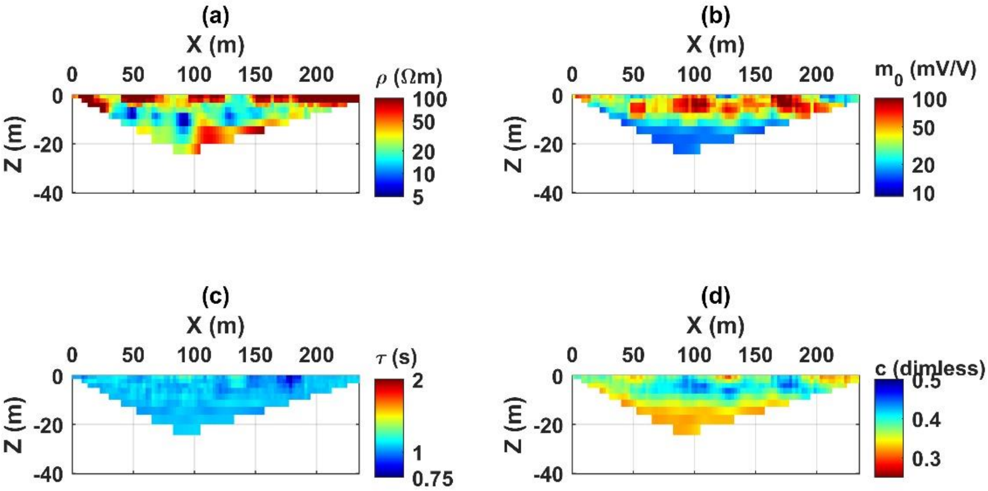

Figure 10. *Cole-Cole spectral inversion of the L4 line. (a) DC resistivity, (b) chargeability, (c) relaxation time, (d) frequency-exponent. RMS error is 19.53 mV for DC voltage and 0.59 mV for IP voltage. Vertical exaggeration is 2.*

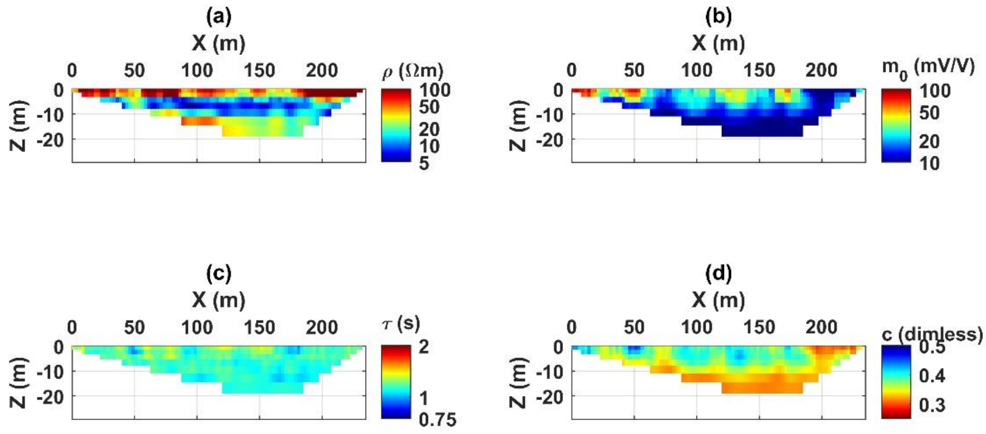

Figure 11. *Cole-Cole spectral inversion of the L5 line. (a) DC resistivity, (b) chargeability, (c) relaxation time, (d) frequency-exponent. RMS error is 17.67 mV for DC voltage and 0.43 mV for IP voltage. Vertical exaggeration is 2.*

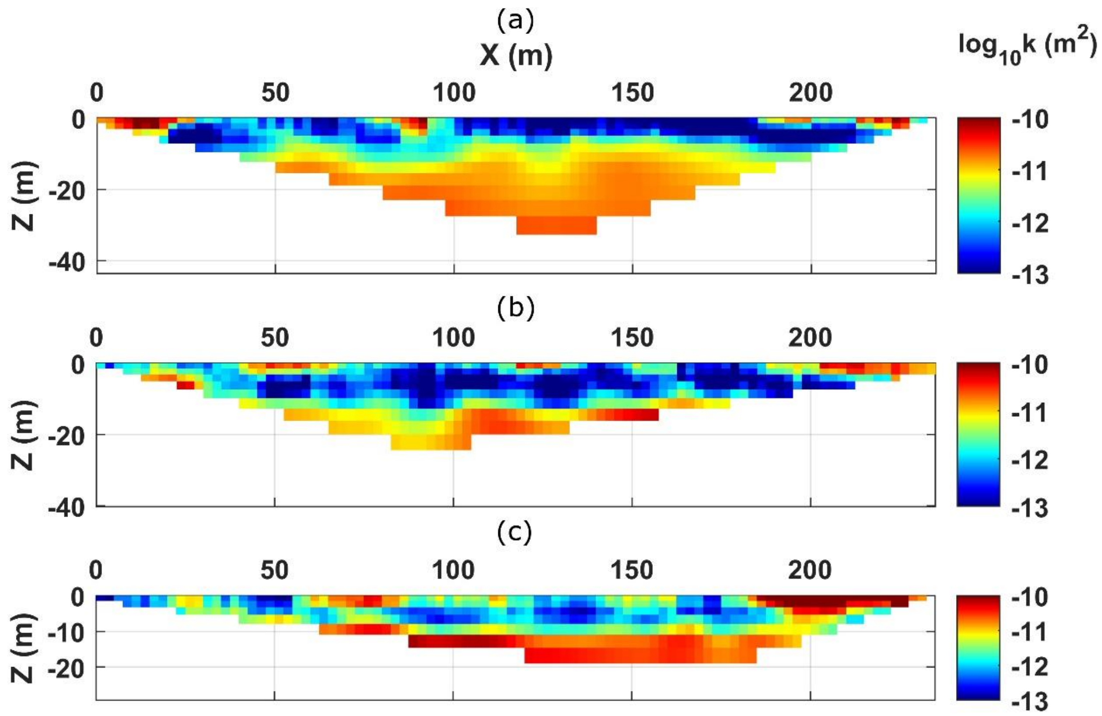

Figure 12. *Permeability sections computed using the prediction after Weller et al. (2015): (a) L3, (b) L4, (c) L5.*